Advanced Energy Conversion Materials
http://ojs.wiserpub.com/index.php/AECM/

Research Article

Band Gap Engineering of Spin-Coated α-Fe_2O_3 for Solar Water Splitting Utilizing a Facile Zinc Doping Route

Md. Ataur Raman[1], Md. Ferdouse Rahman[2], Abu Bakar Md. Ismail[3*]

[1]Department of Computer Science and Engineering, Pundra University of Science and Technology, Bogura, Bangladesh
[2]Department of Electrical & Electronic Engineering, Begum Rokeya University, Rangpur, Bangladesh
[3]Department of Electrical and Electronic Engineering, University of Rajshahi, Rajshahi-6205, Bangladesh
E-mail: rubon.abm.ismail@gmail.com

Received: 14 August 2024; **Revised:** 26 September 2024; **Accepted:** 26 September 2024

Graphical Abstract

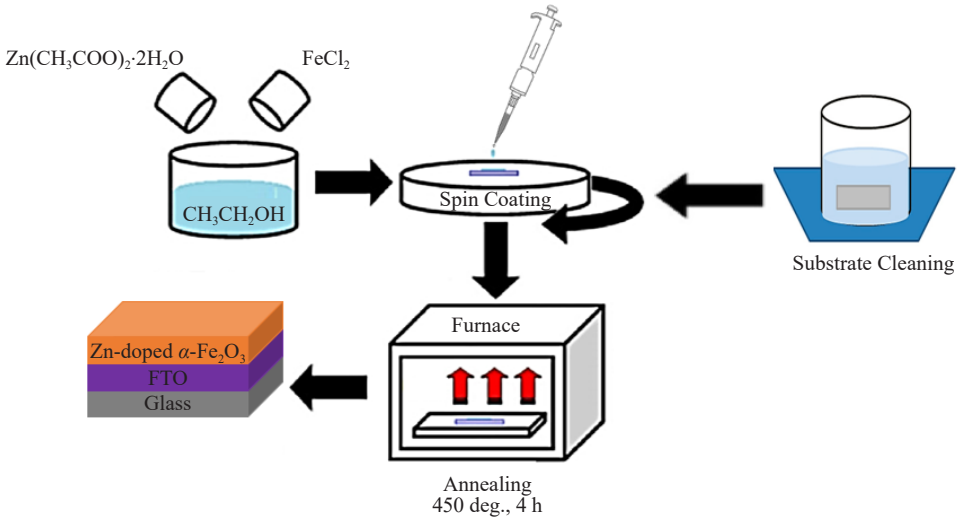

Abstract: Iron oxide (hematite, α-Fe_2O_3) is an earth-abundant material having a favorable band gap for solar energy harvesting by producing Hydrogen (H_2) by photoelectrochemical (PEC) water splitting. Although Fe_2O_3 has a valence band maximum (VBM) more positive than the water oxidation potential in the normalized hydrogen energy scale (NHE), it can not be used as a photocathode because of the more positive conduction band minima (CBM) than the reduction potential of the electrons required for the hydrogen evolution reaction (HER). This paper reports the band gap engineering of Fe_2O_3 by doping it with Zinc (Zn) through a facile way to modify its CBM and VBM to enable it to work as an ideal and efficient photocatalyst. One-pot synthesis of α-Fe_2O_3 doped with Zn was achieved by spin-coating a precursor solution prepared with $FeCl_2$ and Zinc acetate ($Zn(CH_3COO)_2{\cdot}2H_2O$) on fluorine-doped tin oxide (FTO) or glass substrates. The films were then annealed in air at around 450 °C. The surface morphology and the crystal structure

DOI: https://doi.org/10.37256/aecm.5220245492

of the Fe_2O_3 were studied using SEM (Scanning Electron Microscope) and XRD (X-ray diffractometer). The UV-VIS spectrophotometry and spectroelectrochemistry (SEC) determined the band energies of α-Fe_2O_3 and Zn-doped α-Fe_2O_3. The band gap and CBM of pristine α-Fe_2O_3 were found to be ~ 2.09 eV and -5.31 eV vs. E_{VAC}, whereas the band gap and CBM of Zn-doped α-Fe_2O_3 were ~ 1.96 eV and -4.3 eV vs. E_{VAC} respectively. The outcome of the photoelectrochemical study shows that α-Fe_2O_3 doped with Zn can have a reduced band gap with more negative CBM than the H^+/H_2 reduction potential that efficiently ensures both oxygen and hydrogen evolution reaction.

***Keywords*:** hematite, conduction band, valence band, photocatalyst, Zinc doping

1. Introduction

The importance of semiconductors in chemical and industrial processes impelled an extensive research effort to understand the fundamentals of photochemical processes and to develop new photocatalysts. Photocatalysts can enhance processes such as the photoinduced decomposition of organic and inorganic contaminants [1-2], the photoinduced decomposition of water to hydrogen and oxygen [3], etc. In contrast, for producing oxygen and hydrogen from water and sunlight, chemical methods are promising options for combining design simplicity with high energy density [4]. One possible way of achieving energy sustainability is water splitting using solar radiation [5]. Solar water splitting may be of two types, e.g., one involves a linked solar cell-water electrolysis system, while the other involves the direct setup of photoelectrochemical (PEC) cells. The second method outperforms the first in terms of efficiency and costs because it integrates the electrolyzer and solar cell into a single system [6-7]. Renowned researchers Fujishima and Honda first experimented on PEC water splitting using TiO_2 as the photocatalyst in 1976 [8]. Researchers have been trying to develop implementable water splitting systems. These days, PEC water splitting is the main focus of research. Because of their unique physicochemical characteristics and advantageous band location, semiconductor materials are highly desirable in solar water splitting. Considering this, iron oxide (hematite, α-Fe_2O_3) stands out as one of the most promising candidates for photoelectrochemical (PEC) water oxidation among various semiconductor materials, including $BiVO_4$ [9], WO_3 [10], ZnO [11], and TiO_2 [12]. This is attributed to its favorable band gap of around 2.2 eV, remarkable responsiveness to visible light, cost-effectiveness, photocatalytic stability, non-toxic nature, and abundance in the earth's crust [13-14]. Given that α-Fe_2O_3 exhibits n-type characteristics, it is likely to demonstrate considerable photocatalytic activity. However, its performance is constrained by inadequate conductivity and a high rate of electron-hole recombination [15]. A significant limitation of α-Fe_2O_3 is that the position of its conduction band is situated below the H^+/H_2 redox potential, which obstructs the spontaneous splitting of water under visible light irradiation, necessitating the application of a voltage bias [5]. The band edge positions of different metal oxides play a crucial role in influencing both water splitting and the generation of photoinduced reactive oxygen species (ROS) [16]. For photocatalysts to effectively facilitate water splitting, it is essential that their CBM is more negative than the H^+/H_2 level relative to the normal hydrogen electrode (E_{NHE}), and that their VBM is more positive than the H_2O/O_2 level relative to E_{NHE}. This condition ensures that the reaction is energetically favorable, enabling photo-excited electrons in the conduction band to effectively reduce H^+ and produce H_2 [6]. Thus, understanding the CBM and VBM band edge locations of semiconductors is crucial for creating novel photocatalysts [17]. Researchers have explored the doping of foreign elements and the synthesis of various nanoscale morphologies to address these challenges. In light of these emerging difficulties, cationic dopants such as Ca^{2+} [18], Mg^{2+} [19], Zn^{2+} [20], and Cu^{2+} [21] have been proposed to achieve p-type conduction in hematite, owing to their remarkable stability in aqueous solutions underwater reduction conditions. A hydrothermal method was employed to synthesize flower-like nanostructures of Cu-doped hematite, which exhibited effective photocathodic activity, despite minimal alteration of the CBM in relation to the H^+/H_2 redox potential [22]. A thermodynamically favorable shift in the CBM was observed in a thin film of N and Zn co-doped hematite, which was deposited using RF reactive magnetron sputtering, leading to the production of photocathodic hydrogen [23]. These examples clearly indicate that the divalent Zn dopant plays a significant role in the formation of a p-type hematite-based photocathode.

This article presents a straightforward, cost-effective method for creating nanostructured hematite films doped with adjustable levels of Zn. Zn, a 3d transition metal, is chosen for its ability to enhance the photoelectrochemical

(PEC) activity of hematite (α-Fe_2O_3) [24-28]. Zn doping has been shown to increase the flat band potential, the charge carrier depletion layer width at the semiconductor-electrolyte junction [26], and the acceptor density [27]. The disorder introduced in the α-Fe_2O_3 lattice by Zn doping [28] has been linked to improved PEC performance. However, the specific modifications to band energies from Zn doping have not been extensively explored. This article investigates these changes in band energies and their contribution to the enhanced PEC performance. A thin film of Zn-doped α-Fe_2O_3 was produced via spin coating and subsequent annealing in air. Spectroelectrochemical and UV-VIS measurements were conducted to estimate the VBM. The findings indicated that the CBM shifted more negatively in relation to the H^+/H_2 reduction potential with Zn doping, with this shift being dependent on the Zn concentration, which needs further investigation.

2. Experimental section

2.1 *Preparation of thin films*

Pristine and Zn-doped Fe_2O_3 were synthesized using a straightforward one-pot spin-coating technique. At first sodalime glass and fluorine-doped tin oxide (FTO)-coated glass substrates measuring 1 × 1 inch were ultrasonically cleaned through sequential steps that included sonication in soapy water followed by isopropyl alcohol. Later substrates were cleaned using acetone and deionized water. Subsequently, the substrates were dried using hot air. The substrate was converted to hydrophilic through a chemical cleaning process involving a piranha solution composed of a 5:1 ratio of H_2SO_4 to H_2O_2 for Fe_2O_3 deposition.

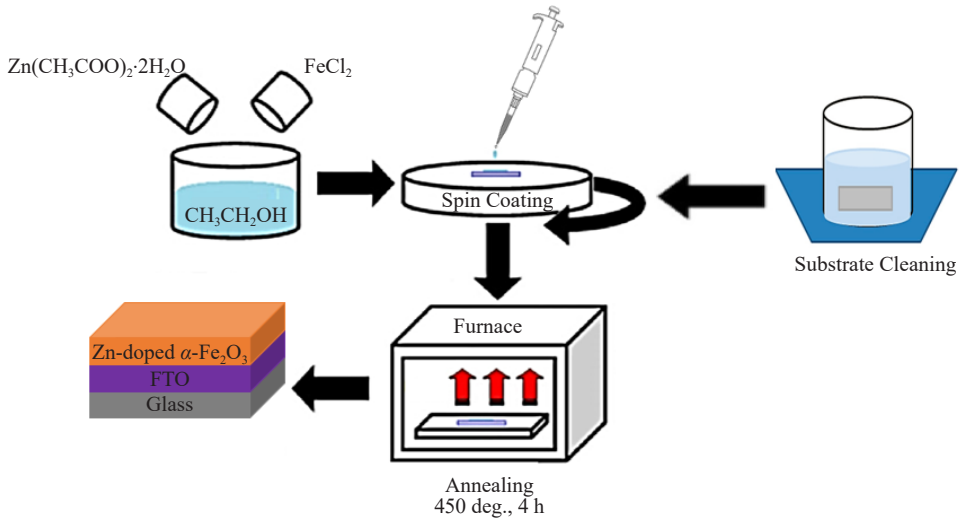

Figure 1. Schematic representation of Zn-doped α-Fe_2O_3 thin film synthesis

To synthesize the pristine Fe_2O_3, 100 wt.% $FeCl_2$ and ethanol solution were blended and stirred to prepare the precursor solution. On the other hand, to synthesize Zn-doped Fe_2O_3, a precursor solution was prepared with 98 wt.% $FeCl_2$ and 2 wt.% zinc acetate ($Zn(CH_3COO)_2{\cdot}2H_2O$). 15µL of the precursor solution was taken in a micropipette and dropped on the substrate surface. The substrates were rotated at a speed of 5,000 rpm (revolutions per minute). Figure 1 depicts the schematic illustration of the production of Zn-doped Fe_2O_3 thin films. Three different thicknesses (5, 7, and 9 layers) of films were investigated in this study. Following the deposition of one layer, the films were allowed to dry in ambient air before a subsequent layer was applied. The prepared film was then annealed for four hours at 450 °C for 4 hours.

2.2 *Film characterization*

Scanning Electron Microscopy (SEM) was employed to analyze the surface morphology of both α-Fe_2O_3 and Zn-doped α-Fe_2O_3. The crystal structures of these materials were investigated using X-ray Diffraction (XRD) with Cu-Kα radiation, covering a 2θ range of 10-70° at a scan speed of 2°/min. The chemical structures of the as-deposited films were assessed through Fourier Transform Infrared Spectroscopy (FT-IR), which operated within a wave number range of 225 to 4,000 cm^{-1}. Prior to FT-IR analysis, the films were held in the holder for four to five minutes to eliminate unwanted H_2O and CO_2. Hall measurements were conducted to determine the conduction types of both α-Fe_2O_3 and Zn-doped α-Fe_2O_3, utilizing a fixed source voltage of 10 V and a magnetic field of 1 T. These measurements confirmed n-type conduction for pure Fe_2O_3 and p-type conduction for the Zn-doped variant. To explore the optical properties of α-Fe_2O_3 and Zn-doped Fe_2O_3, including transmittance and absorbance, a T-60 UV-VIS spectrophotometer was utilized at room temperature, covering a spectrum range of 380-1,000 nm. Additionally, UV-VIS spectroelectrochemistry (SEC) was employed to investigate the band energies of both α-Fe_2O_3 and its Zn-doped counterpart.

3. Results and discussion

3.1 *Structural and morphological analysis*

SEM analysis investigated the nature and morphology of the nanoparticles. Figure 2 presents the surface morphology of 0.5 wt.% Zn-doped α-Fe_2O_3 and 2 wt.% Zn-doped α-Fe_2O_3 as were observed by the SEM. The images reveal a compact particle presence with a dense structure, and the surface layer is uniformly covered with similarly sized granular grains.

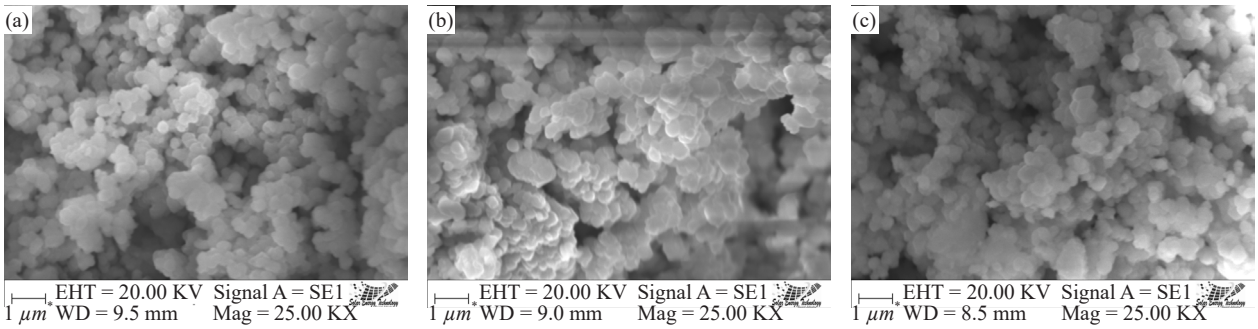

Figure 2. SEM image of (a) pristine α-Fe_2O_3 (b) 0.5 wt.% Zn-doped α-Fe_2O_3 and (c) 2 wt.% Zn-doped α-Fe_2O_3

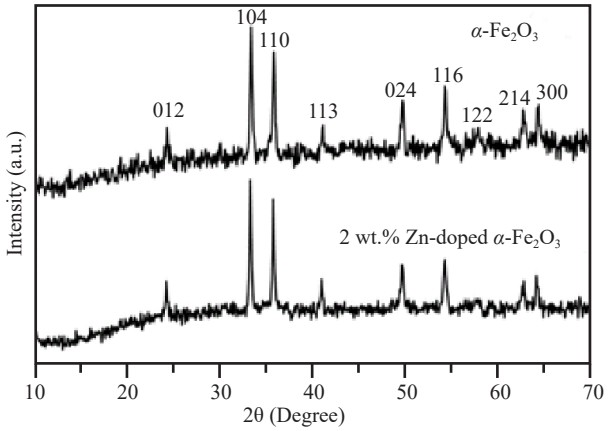

Figure 3. XRD pattern for pristine α-Fe_2O_3 and 2 wt.% Zn-doped α-Fe_2O_3

XRD analysis was employed to verify the structural and phase characteristics of the pristine α-Fe_2O_3 and 2 wt.% Zn-doped α-Fe_2O_3, as illustrated in Figure 3. XRD was performed at a 2θ scan range from 0 to 70°. The analysis reveals the presence of eight distinct sharp peaks corresponding to various crystal orientations, which distinctly indicate the polycrystalline nature of both α-Fe_2O_3 and Zn-doped α-Fe_2O_3.

The principal diffraction peaks are located at 2θ angles of 24.44°, 33.39°, 35.96°, 41.11°, 49.80°, 54.23°, 62.74°, and 64.34°, which can be associated with the (012), (104), (110), (113), (024), (116), (214), and (300) facets of the rhombohedral hematite structure α-Fe_2O_3 (JCPDS card no: 33-0664) [29-31]. Additional studies on similar crystallization processes [32-33] indicate that Zn is uniformly distributed within the crystalline matrix of α-Fe_2O_3. Among the eight peaks, the peak corresponding to the (104) plane is the most prominent, suggesting the formation of the hematite phase [34]. All observed peaks align with the anticipated rhombohedral structural configuration of α-Fe_2O_3. When Zn is introduced into α-Fe_2O_3, no new diffraction peaks rather than α-Fe_2O_3 were indicated in XRD spectra, suggesting that Zn atoms were incorporated in α-Fe_2O_3 matrices. Hence, dopant atoms alter the crystallinity of α-Fe_2O_3 without altering its rhombohedral structure. Debye Scherrer's formula [35] was applied for the calculation of the average crystal size of the sample.

$$\text{Average crystalline size, } D = 0.9\lambda/\beta \cos\theta$$

Where λ represents X-ray wavelength, β represents FWHM (Full Width at Half Maximum) along (104) plane and θ is the diffraction angle. From the (104) peak using Scherrer's equation the mean grain size was 34.58 nm.

EDX analysis is essential for confirming the presence of Zn in Zn-doped α-Fe_2O_3. Table 1 and Figure 4 provide EDX elemental composition data, showing peaks for iron, oxygen, and Zn. This study verifies the incorporation of Zn in the Zn-doped α-Fe_2O_3.

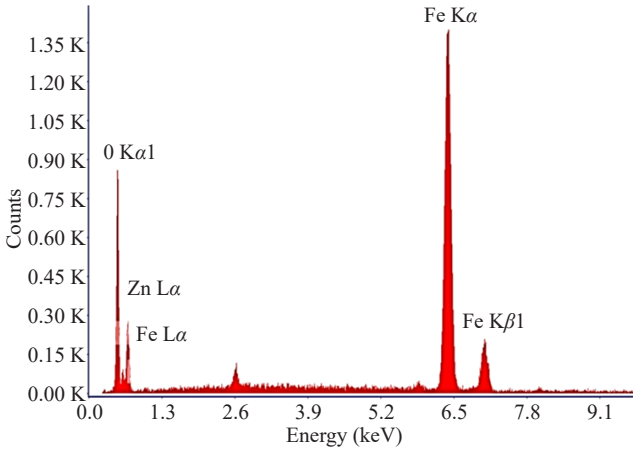

Figure 4. EDX spectra for 2% Zn-doped α-Fe_2O_3

Table 1. Elemental composition of 2% Zn doped α-Fe_2O_3

Element	Wt%	At%
O	15.2	16.3
Fe	82.9	81.9
Zn	1.9	1.8

3.2 *Optical analysis*

The band gap energy is determined using. The band gap energy of both pristine and Zn-doped α-Fe_2O_3 films was estimated using optical absorption data. The Tauc plots were created by calculating $(\alpha h\upsilon)^n$ from the absorption data using the following formula and plotting against $h\upsilon$. The extrapolation of the linear region on the energy axis of the Tauc plot estimated the band gap as shown in Figure 5.

$$(\alpha h\upsilon)^n = B(h\upsilon - E_g)$$

In this equation, α denotes the absorption coefficient, $h\upsilon$ represents the photon energy, B is a constant, E_g signifies the band gap energy, and n indicates the type of transition (with $n = 2$ for direct transitions and $n = 1/2$ for indirect transitions). The indirect band gap energies for both pristine and Zn-doped α-Fe_2O_3 films are given in Table 2.

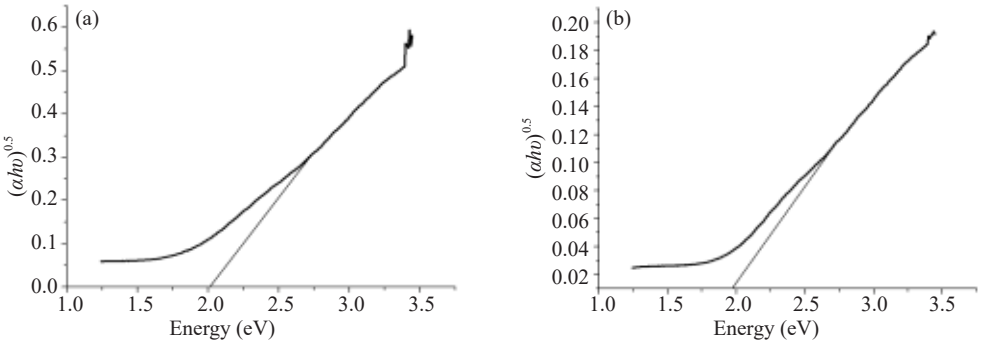

Figure 5. Tauc plots for (a) pristine and (b) for 2% Zn-doped α-Fe_2O_3

Table 2. The band gap energies of pristine and doped α-Fe_2O_3

Sample	Band gap energy (eV)
pristine α-Fe_2O_3	2.09
Zn-doped α-Fe_2O_3	1.96

The indirect band gap of pristine α-Fe_2O_3 ranges from 1.38 to 2.09 eV [36]. Our results align closely with this reported value. Doping with 2 wt. % Zn further reduced the band gap to 1.96 eV, a phenomenon previously documented and explained [37]. Similar reductions in band gap have also been observed both theoretically and experimentally for metal doping in transition metal sulfides and oxides [38, 39].

3.3 *Spectroelectrochemical analysis*

To determine the frontier orbital energies, specifically the CBM and VBM of pristine and Zn-doped α-Fe_2O_3 thin films, the potential-dependent UV-VIS spectroelectrochemical method was employed. This method offers a straightforward and effective experimental approach for ascertaining energy band values. All measurements were conducted in a 0.1 M NaOH aqueous solution, serving as a non-solvent electrolyte. The working electrodes comprised FTO-coated substrates featuring both pristine α-Fe_2O_3 and Zn-doped α-Fe_2O_3. A platinum (Pt) wire measuring 1 × 1 cm^2 was utilized as the counter electrode. Changes in relative absorbance were recorded with a T60 UV-VIS spectrophotometer. The experiments were performed in a two-electrode cell, specifically a quartz cuvette, where the FTO-coated α-Fe_2O_3 acted as the working electrode and the platinum wire served as the counter electrode. The quartz

cuvette was positioned in the spectrophotometer's sample holder, and aligned with the light beam. Potential control was achieved through an external supply, which included a source meter and DC supply.

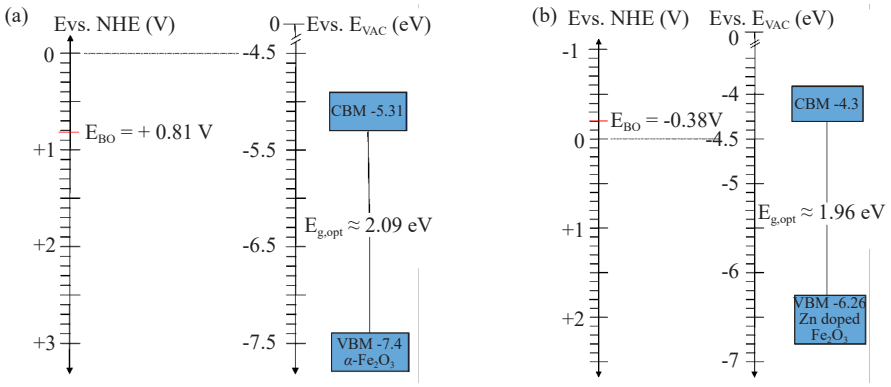

Figure 6. (a) Frontier orbital energy level diagram for pristine α-Fe_2O_3 film on FTO; (b) Frontier orbital energy level diagram for Zn-doped α-Fe_2O_3 film on FTO

The scanning rate of potential was varied between 0.2 and 10 mV s^{-1}. The normalized bleach absorbance at 740 nm was analyzed as a function of the applied potential. The bleaching data aligns well with a sigmoidal function, which distinctly illustrates the saturation of the bleaching effect. These spectroelectrochemical findings contribute to the development of a frontier orbital energy level diagram for both pristine α-Fe_2O_3 and Zn-doped α-Fe_2O_3 films.

The reduction potentials determined electrochemically offer an estimation for the CBM of pristine α-Fe_2O_3, which is approximately -5.31 eV relative to the vacuum level (EVAC), as illustrated in Figure 6. Similarly, the electrochemical analysis provides an estimate for the CBM of Zn-doped α-Fe_2O_3, found to be around -4.3 eV versus EVAC, as depicted in Figure 6. Experimental results indicate that pristine α-Fe_2O_3 functions as a photoanode, given that the CBM edge is situated below the reduction potential. In contrast, Zn-doped α-Fe_2O_3 acts as a photocathode, as its CBM edge is located above the reduction potential. The introduction of Zn^{2+} doping can alter the positions of both the CBM and the VBM by creating new energy levels or modifying existing defect/trap levels within the band gap, leading to shifts in the band edges. These defect states may act as recombination centers for charge carriers, thereby affecting the effective band gap. A theoretical investigation has reported a similar positive shift in the CBM for α-Fe_2O_3 upon Zn doping [40].

4. Conclusions

With a target of engineering the band gap of α-Fe_2O_3 to make it a lower but straddled band so that α-Fe_2O_3 becomes an ideal and efficient photocatalyst capable of performing Hydrogen and Oxygen evolution reactions, a simple one-pot process Zn-doping of α-Fe_2O_3 has been presented and investigated. It is observed from the experimental result that the Zn-doping shifted the CBM edge of Fe_2O_3 to a more negative value than the pristine Fe_2O_3. The negative shift of the conduction band minimum (CBM) was proportional to the doping amount. At a Zn concentration of 2%, it eventually shifted the band edge to more negative than the H^+/H_2 reduction potential, enabling it to work in both photoanode and photocathode. This experimental experience of band gap engineering of Fe_2O_3 by Zn-doping indicates that Zn doping can be an efficient tool for band gap tuning of low-cost metal oxides like Fe_2O_3 required for simultaneous Oxygen and Hydrogen generation.

Data availibility

The corresponding author will make available on request the datasets produced while performing experiments

presented in this article.

Conflict of interest

The authors declare no conflict of interest.

References

[1] Serpone N, Lawless D, Terzian R, Minero C, Pelizzetti E. Heterogeneous photocatalysis: photochemical conversion of inorganic substances in the environment: hydrogen sulfide, cyanides, and metals. In: Pelizzetti E, Schiavello M. (eds.) *Photochemical Conversion and Storage of Solar Energy: Proceedings of the Eighth International Conference on Photochemical Conversion and Storage of Solar Energy.* Palermo, Italy. Springer Netherlands; 1991. p.451-475.

[2] Brinkley D, Engel T. Photocatalytic dehydrogenation of 2-propanol on TiO_2 (110). *The Journal of Physical Chemistry B*. 1998; 102(39): 7596-7605.

[3] Lauermann I, Meissner D, Memming R. The problem of light-induced oxygen production at catalyst-loaded CdS suspensions. *Journal of Electroanalytical Chemistry and Interfacial Electrochemistry*. 1987; 228(1-2): 45-53.

[4] George KEN. *Characterization of Iron Oxide Thin Films for Photoelectrochemical Hydrogen Production*. UNLV Theses, Dissertations, Professional Papers, and Capstones; 2009.

[5] Bak T, Nowotny J, Rekas M, Sorrell CC. Photo-electrochemical hydrogen generation from water using solar energy. Materials-related aspects. *International Journal of Hydrogen Energy*. 2002; 27(10): 991-1022.

[6] Grätzel M. Photoelectrochemical cells. *Nature*. 2001; 414(6861): 338-344.

[7] Kim JY, Magesh G, Youn DH, Jang JW, Kubota J, Domen K, et al. Single-crystalline, wormlike hematite photoanodes for efficient solar water splitting. *Scientific Reports*. 2013; 3(1): 2681.

[8] Fujishima A, Honda K. Electrochemical photolysis of water at a semiconductor electrode. *Nature*. 1972; 238(5358): 37-38.

[9] Qi Y, Zhang J, Kong Y, Zhao Y, Chen S, Li D, et al. Unraveling of cocatalysts photodeposited selectively on facets of $BiVO_4$ to boost solar water splitting. *Nature Communications*. 2022; 13(1): 484.

[10] Pehlivan IB, Atak G, Niklasson GA, Stolt L, Edoff M, Edvinsson T. Electrochromic solar water splitting using a cathodic WO_3 electrocatalyst. *Nano Energy*. 2021; 81: 105620.

[11] Cao C, Zhang B, Lin S. p-type ZnO for photocatalytic water splitting. *APL Materials*. 2022; 10(3): 030901

[12] Khan SUM, Al-Shahry M, Ingler Jr WB. Efficient photochemical water splitting by a chemically modified n-TiO_2. *Science*. 2002; 297(5590): 2243-2245.

[13] Petroleum B. *Bp Statistical Review of World Energy June 2013*. London: British Petroleum; 2013.

[14] Kay A, Cesar I, Grätzel M. New benchmark for water photooxidation by nanostructured α-Fe_2O_3 films. *Journal of the American Chemical Society*. 2006; 128(49): 15714-15721.

[15] Jorand Sartoretti C, Alexander BD, Solarska R, Rutkowska IA, Augustynski J, Cerny R. Photoelectrochemical oxidation of water at transparent ferric oxide film electrodes. *The Journal of Physical Chemistry B*. 2005; 109(28): 13685-13692.

[16] Li Y, Zhang W, Niu J, Chen Y. Mechanism of photogenerated reactive oxygen species and correlation with the antibacterial properties of engineered metal-oxide nanoparticles. *ACS Nano*. 2012; 6(6): 5164-5173.

[17] Wu Y, Chan MKY, Ceder G. Prediction of semiconductor band edge positions in aqueous environments from first principles. *Physical Review B-Condensed Matter and Materials Physics*. 2011; 83(23): 235301.

[18] Yu Q. *Construction of Hematite-based Photoelectrochemical Cells for Visible Light Water Splitting*. Hokkaido University; 2016.

[19] Lin Y, Xu Y, Mayer MT, Simpson ZI, McMahon G, Zhou S, et al. Growth of p-type hematite by atomic layer deposition and its utilization for improved solar water splitting. *Journal of the American Chemical Society*. 2012; 134(12): 5508-5511.

[20] Qi X, She G, Wang M, Mu L, Shi W. Electrochemical synthesis of p-type Zn-doped α-Fe_2O_3 nanotube arrays for photoelectrochemical water splitting. *Chemical Communications*. 2013; 49(51): 5742-5744.

[21] Meng XY, Qin GW, Li S, Wen XH, Ren YP, Pei WL. Enhanced photoelectrochemical activity for Cu and Ti doped hematite: The first principles calculations. *Applied Physics Letters*. 2011; 98(11): 112104

[22] Tsege EL, Atabaev TS, Hossain MA, Lee D, Kim HK, Hwang YH. Cu-doped flower-like hematite nanostructures

for efficient water splitting applications. *Journal of Physics and Chemistry of Solids*. 2016; 98: 283-289.
[23] Sekizawa K, Oh-ishi K, Kataoka K, Arai T, Suzuki TM, Morikawa T. Stoichiometric water splitting using a p-type Fe_2O_3 based photocathode with the aid of a multi-heterojunction. *Journal of Materials Chemistry A*. 2017; 5(14): 6483-6493.
[24] Mirbagheri N, Wang D, Peng C, Wang J, Huang Q, Fan C. Visible light driven photoelectrochemical water oxidation by Zn-and Ti-doped hematite nanostructures. *Acs Catalysis*. 2014; 4(6): 2006-2015.
[25] Xi L, Bassi PS, Chiam SY, Mak WF, Tran PD, Barber J, et al. Surface treatment of hematite photoanodes with zinc acetate for water oxidation. *Nanoscale*. 2012; 4(15): 4430-4433.
[26] Kumari S, Tripathi C, Singh AP, Chauhan D, Shrivastav R, Dass S, et al. Characterization of Zn-doped hematite thin films for photoelectrochemical splitting of water. *Current Science*. 2006; 91(8): 1062-1064.
[27] Ingler Jr WB, Baltrus JP, Khan SUM. Photoresponse of p-type zinc-doped iron (III) oxide thin films. *Journal of the American Chemical Society*. 2004; 126(33): 10238-10239.
[28] Chen YC, Kuo CL, Hsu YK. Facile preparation of Zn-doped hematite thin film as photocathode for solar hydrogen generation. *Journal of Alloys and Compounds*. 2018; 768: 810-816.
[29] Souza FL, Lopes KP, Nascente PAP, Leite ER. Nanostructured hematite thin films produced by spin-coating deposition solution: Application in water splitting. *Solar Energy Materials and Solar Cells*. 2009; 93(3): 362-368.
[30] Cuong ND, Hoa TT, Khieu DQ, Hoa ND, Van Hieu N. Gas sensor based on nanoporous hematite nanoparticles: effect of synthesis pathways on morphology and gas sensing properties. *Current Applied Physics*. 2012; 12(5): 1355-1360.
[31] Cao RB, Chen XQ, Shen WH, Long Z. A facile route to synthesize nano-hematite colloid. *Materials Letters*. 2011; 65(21-22): 3298-3300.
[32] Yang S, Huang Z, Wu P, Li Y, Dong X, Li C, et al. Rapid removal of tetrabromobisphenol A by α-Fe_2O_{3-x}@ Graphene@ Montmorillonite catalyst with oxygen vacancies through peroxymonosulfate activation: Role of halogen and α-hydroxyalkyl radicals. *Applied Catalysis B: Environmental*. 2020; 260: 118129.
[33] Arman IS, Rahman MA, Ismail ABM. Electrical and morphological characterization of zinc-doped α-Fe_2O_3 thin films at different annealing temperature. *Journal of Materials Research and Technology*. 2019; 8(6): 5909-5915.
[34] Anandan S, Muthukumaran S, Ashokkumar M. Modifications in band gap and optical properties of $Zn_{0.96-x}Nd_{0.04}Cu_xO$ (x = 0, 0.05, 0.1 and 0.15) nanoparticles. *Journal of Sol-Gel Science and Technology*. 2014; 70: 133-141.
[35] Kumar V, Chahal S, Singh DS, Kumar A, Kumar P, Kandasami A. Annealing effect on the structural and dielectric properties of hematite nanoparticles. *AIP Conference Proceedings*. 2018; 1953(1): 030245.
[36] Satheesh R, Vignesh K, Suganthi A, Rajarajan M. Visible light responsive photocatalytic applications of transition metal (M = Cu, Ni and Co) doped α-Fe_2O_3 nanoparticles. *Journal of Environmental Chemical Engineering*. 2014; 2(4): 1956-1968.
[37] Suman, Chahal S, Kumar A, Kumar P. Zn doped α-Fe_2O_3: An efficient material for UV driven photocatalysis and electrical conductivity. *Crystals*. 2020; 10(4): 273.
[38] Taoufiq M, Soussi A, Elfanaoui A, Baoubih S, Ihlal A, Bouabid K. DFT theoretical and experimental investigations of the effect of Cu doping within SILAR deposited ZnS. *Optical Materials*. 2024; 147: 114607.
[39] Soussi A, Haounati R, Ait hssi A, Taoufiq M, Asbayou A, Elfanaoui A, et al. First principle study of structural, electronic, optical properties of Co-Doped ZnO. *Journal of Composites Science*. 2023; 7(12): 511.
[40] Simfukwe J, Mapasha RE, Braun A, Diale M. Exploring the stability and electronic properties of Zn-doped hematite surfaces for photoelectrochemical water splitting. *Journal of Physics and Chemistry of Solids*. 2020; 136: 109159.